Article:
Terzioglu, F. and Rongong, J.A. (2026) Particle shape dependent energy dissipation behaviour of granular dampers with circular toroid particles. Powder Technology. 122819. ISSN: 0032-5910

https://doi.org/10.1016/j.powtec.2026.122819

Particle shape dependent energy dissipation behaviour of granular dampers with circular toroid particles

Authors and affiliations

Furkan Terzioglu[(1)*]

Jem Athing Rongong[(2)]

[(1)*] furkan.terzioglu@iuc.edu.tr – Department of Mechanical Engineering, Faculty of Engineering, Istanbul University-Cerrahpasa, Istanbul, Turkiye

[(2)] j.a.rongong@sheffield.ac.uk – School of Mechanical, Aerospace and Civil Engineering, University of Sheffield, Mappin Street, S1 3JD, Sheffield, United Kingdom

Abstract

The energy dissipation effectiveness of a granular damper shows high performance in two motional phases. It is shown that particle shape affects one of these phases, the bouncing bed. A parallel study using experiments and Discrete Element Method simulations involving circular toroidal particles is used to evaluate the effect of particle shape on the non-linear energy dissipation over a wide range of excitation frequencies and amplitudes. The results show that the excitation amplitude that provides optimum bouncing-bed performance can be increased above that for spherical particles using high-sphericity toroidal ones. Further deviations in shape (reducing sphericity) reduce this level below that for spheres. This behaviour is related to the packing density achieved and hence the clearance in the enclosure. While small spheres can achieve random close packing and slight deviation in shape allows denser arrangements, large shape deviations can reduce the packing density significantly. For the other motional phase, fluidisation, which occurs at lower amplitudes, particle shape does not have a significant effect. This is attributed to the motional behaviour that involves compaction and decompaction every cycle and is dominated by local interactions at the contact points between individual particles.

Keywords

granular damping; particle damping; particle shape; circular toroid; discrete element method; bouncing-bed and fluidisation phases

Highlights

- Multi-sphere approximation of circular toroid particles for DEM simulations.
- DEM simulations and physical experiments on granular dampers with toroid particles.
- Sphericity of toroidal particles shown to influence parts of the damping performance curve.
- Physical explanation established linking particle shape to dissipative performance in the bouncing bed motional phase.

Graphical abstract

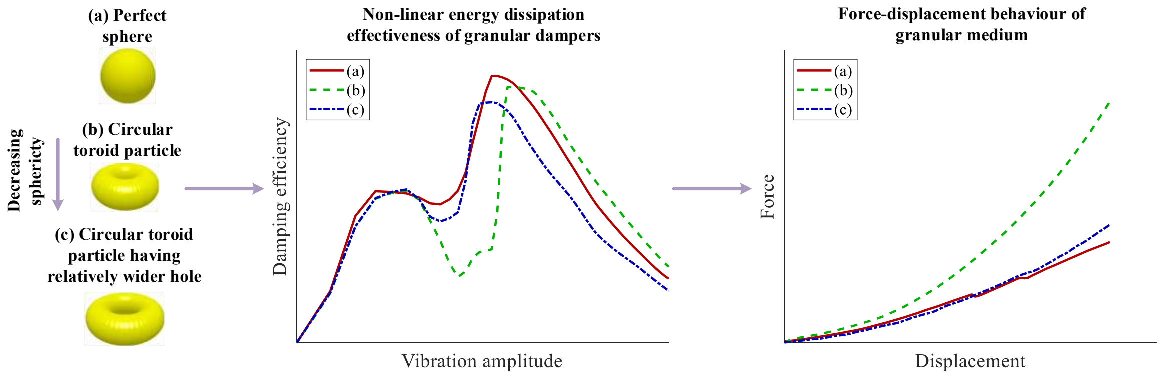

1 Introduction

A typical granular damper is obtained by partially filling with relatively small particles a hollow enclosure that is either attached to or integrated within the host structure. This type of granular fill can provide effective passive vibrational control. The key physical principal to activate the energy dissipation in granular dampers is momentum exchange which accomplishes the transfer of vibrational energy from the structure to the particles. The transmitted energy is dissipated through collisional and frictional interactions amongst the particles, and between the particles and the surrounding boundaries of the enclosure.

Despite being physically robust and conceptually simple [1–5], designing a granular damper requires particular care because its energy dissipation characteristic is non-linear and depends on both amplitude and frequency of vibrations [3,6,7]. The main source of this non-linear behaviour is the collective motional state of the vibrating particles which significantly affects the conditions under which collisional and frictional interactions occur. As the operating motional state changes, dramatic alterations can be observed in the granular energy dissipation performance [8–12]. It has been shown that in addition to vibration amplitude and frequency the motional state depends on the volume fill ratio of the cavity [13], particle shape [14], existence or lack of gravity [8] and gravity-to-vibration directional orientation [6,7].

Mapping motional states (or phases) on an amplitude-frequency plane [10,11,15,16] helps to classify the collective motional behaviours observed and to identify transitions between different types of motion. A typical phase map [7], is provided in Figure 1a. To show the link between the motional phase and the energy dissipation performance, the most effective regions are highlighted in this map. The associated motional behaviours of particles in these regions are illustrated in Figure 1b. To show typical granular energy dissipation performance achieved during different motional phases, a measurement recorded at constant frequency (from this dataset [7]) is provided in Figure 1c.

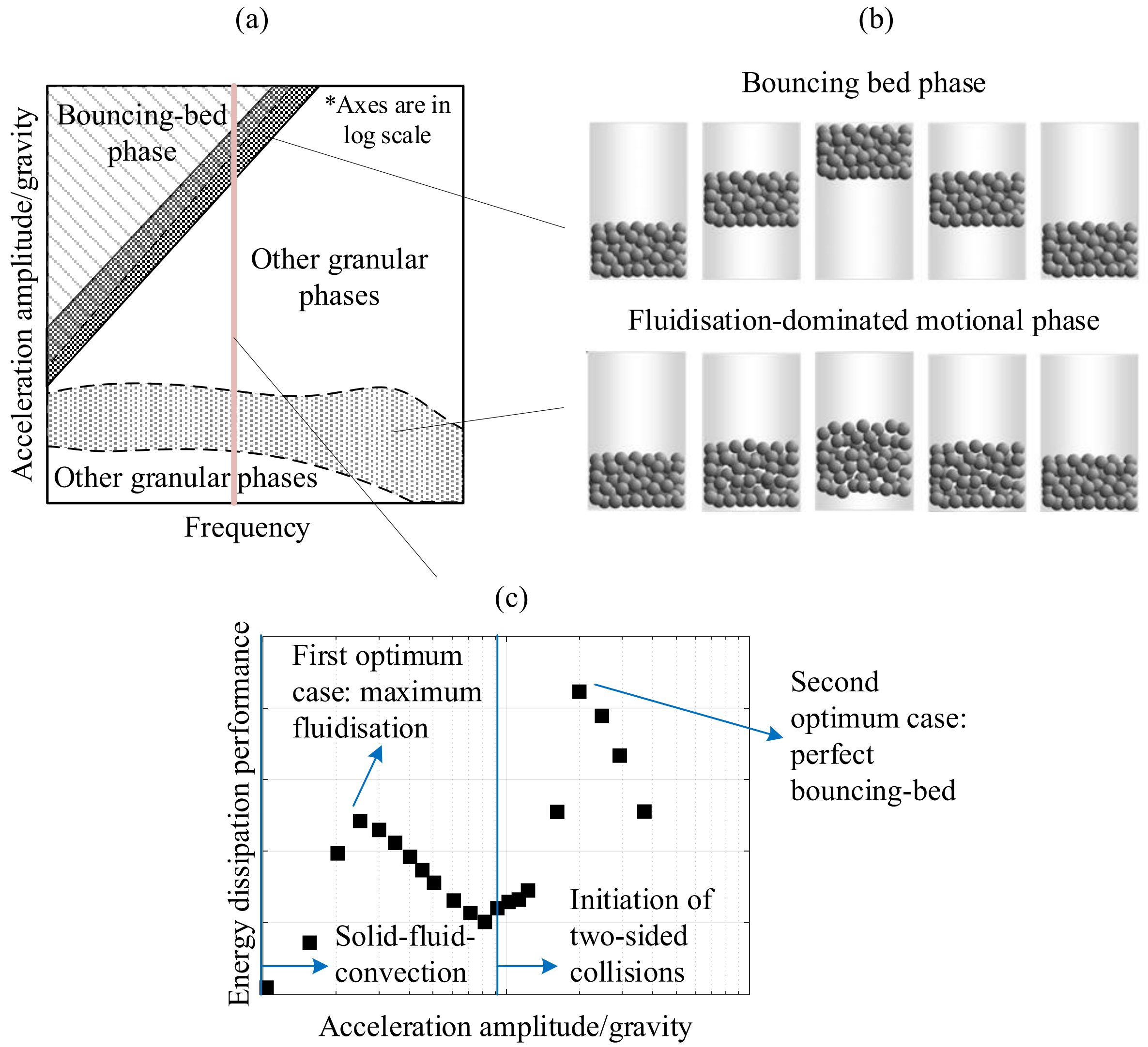

Figure 1: Schematic linking energy dissipation efficiency of a granular damper to collective particle motion: a) typical phase map, b) relative position of particles to the enclosure for different motional states, and c) a sample measurement at a specific frequency [7] producing two optimum behaviours within the investigated amplitude range.

The "bouncing-bed" phase is the most effective motional behaviour for energy dissipation in granular dampers [6,7,9]. As sketched in Figure 1b, in this phase, particles form a compact mass that collides with the enclosure end walls each time the enclosure changes direction. The collective collisions transfer a large amount of momentum to the particles and dissipate vibrational energy through relative motions within the granular medium. This mechanism is most effective if end wall collisions occur at the point in the cycle when the enclosure speed is highest as this maximises the momentum transfer [9, 14]. As performance decreases significantly away from this condition, it is important to be able to predict the optimal conditions [8,17] and to understand the sensitivity to changes in granular damper properties [14]. This optimum case is best suited for high acceleration amplitude, low frequency applications as can be seen from Figure 1.

The other motional phase that provides significant energy dissipation is generally referred to as “fluidisation” in granular damper literature. As illustrated in Figure 1b, this motional phase involves the cyclic compaction and decompaction of the body of particles without significantly altering the relative positions and contacts of individual particles. This motion facilitates energy dissipation through relative movements between adjacent particles. Fluidisation begins where vibration-induced inertial forces exceed the stabilising forces of weight and static friction. As intensity increases, fluidisation spreads throughout the medium, increasing energy dissipation. The most effective energy dissipation is achieved around the fluidisation optimum [7], which can be seen from Figure 1a to cover a broad frequency range at relatively low acceleration amplitude. Beyond this point, increased vibration leads to convection, where particles de-compact and lose relative positioning which results in reduced energy dissipation effectiveness.

Factors that influence the damping performance in these two motional phases have been widely reported elsewhere in the literature and are not detailed here. Instead, some points of direct relevance to the work presented in this paper are highlighted below to provide context for the approach followed.

- The maximum energy dissipation that can be achieved is proportional to the mass of particles,
- Energy dissipation is relatively insensitive to orientation with respect to gravity for these motional phases,
- Energy is dissipated through friction and inelastic impacts. While the relative contribution varies continuously throughout each vibration cycle, depending on the

instantaneous dynamics of the particles [15,18], sliding friction typically accounts for three quarters of the time-averaged dissipation.

- Moderate adjustments to the energy loss within particles (often accounted for using the coefficient of restitution, CoR) have little effect on the overall performance. Reducing energy lost directly during an impact (by increasing the CoR) increases the losses arising from sliding friction, so the effect on the overall level is insignificant.

The importance of particle shape on energy dissipation performance has largely been neglected in the granular damping literature with most studies using spherical particles. A few quantitative studies have been reported involving particles generated from connected spheres [19], 2-dimensional polygons[20] cylinders and cubes [21]. The effects observed remain specific to the configurations considered and sometimes do not match experimental observations. A recent combined numerical/experimental study that used spheroidal particles revealed that their sphericity affects the amplitude at which the bouncing bed phase forms [14]. Reduced sphericity was shown to correlate with an increase in vibration intensity needed to achieve the optimal bouncing bed. Particle sphericity was then linked to packing density and stiffness of the granular medium, resulting in the conclusion that increased shear stiffness of the granular medium increases amplitude for optimum performance.

For designers interested in using non-spherical particles, there is no consistent guidance on the effect that sphericity has on fluidisation/convection behaviour. Additionally, previous investigations involving the bouncing bed were limited to only spheroidal particles [14]. To address this knowledge gap, therefore, the aim of this work is to evaluate the influence of non-spherical particles on the energy dissipation performance of granular dampers, with particular focus on the optimum conditions for fluidisation and bouncing-bed motional phases. The particles used in this investigation have a circular toroidal geometry which produce different packing structures to the spheroids studied previously [14], and therefore allow studying the generality of conclusions relating to the shape dependence of granular energy dissipation efficiency. Circular toroids can be defined analytically and manufactured for a range of sphericities, enabling a systematic investigation of non-spherical particles whilst maintaining consistent volume and mass.

A discrete element method (DEM) approach validated by physical experiments is employed to simulate the non-linear dissipative behaviour of dampers filled with these particles over a wide range of frequency and amplitude, enabling the determination of shape-dependent variations in the energy dissipation performance. This paper seeks a fundamental understanding of the sensitivity of energy dissipation to particle shape that will guide the designer to use particle shape as a design parameter for practical applications.

2 Methodological approach

In this study, the structure-independent modelling approach was used to focus on the effect of circular toroids on the granular dissipative characteristic rather than increasing complexity by involving the dynamics of an elastic host structure. The model shown in Figure 2 includes the main elements of a granular damper and is used for both numerical and experimental studies.

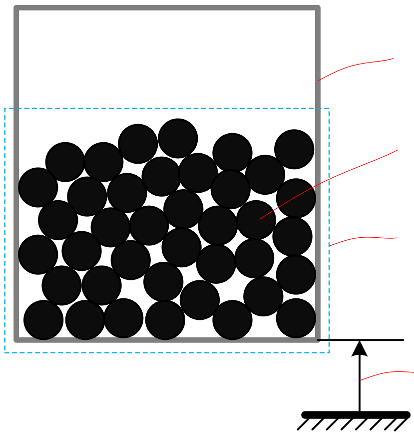

Figure 2: Structure-independent granular damper model.

As directionality does not significantly affect the granular dissipative behaviour for bouncing bed and fluidisation behaviour [7], a vertical design, where gravity was in the same axis as the excitation, was the primary focus for this investigation. The corresponding horizontal design, where the damper and excitation are rotated to be perpendicular to gravity, was also studied but is only reported where the difference is significant and provides additional understanding. The granular medium was excited along this axis by prescribing the harmonic motion of the enclosure as:

$$u = (\Gamma g/\omega^2)\sin(\omega t) \tag{1}$$

where Γ is the non-dimensional acceleration amplitude, g is the gravitational acceleration, ω is the excitation frequency and t is the time.

As the vibrational energy dissipated by a granular damper varies by many orders of magnitude depending on the vibration frequency and amplitude, performance-based investigations were made using a non-dimensional energy dissipation efficiency parameter [6–8] obtained from ratio of the average energy dissipated by the granular damper over a vibration period ($\tilde{E}_{\text{numerical}}$) to the maximum energy that could be dissipated over the same vibration period by an ideal granular damper ($\tilde{E}_{\text{max}}$) of the same mass:

$$\eta_{\text{granular}} = \tilde{E}_{\text{numerical}} / \tilde{E}_{\text{max}} \tag{2}$$

Here, the maximum dissipated energy (which theoretically occurs in the bouncing bed phase and results in optimal momentum transfer) is determined by:

$$\tilde{E}_{\text{max}} = (2\Gamma g/\omega)^2 m_{\text{particle}} \tag{3}$$

where m_{particle} is the total mass of particles. It should be noted that the definition of the maximum dissipated energy is based on reference [8] where it is assumed that all particles collectively collide with both end walls of enclosure at maximum enclosure velocity and these collisions are completely inelastic. The definition is consistent with those used by other authors [22–24] which differ only by a constant scaling factor.

2.1 Circular toroid particle shape

A circular toroid is obtained by sweeping a circle, whose radius is denoted by b_{toroid}, through a circular trajectory that has a radius of a_{toroid}. The two-dimensional view of a circular toroid is shown in Figure 3.

A non-spherical object can be characterised using its sphericity [25,26], ψ, which is the ratio of surface areas of an equal volume sphere to the object in question. For a circular toroid this becomes,

$$\psi = \sqrt[3]{9 b_{\text{toroid}} / (4\pi a_{\text{toroid}})} \tag{4}$$

To achieve a comprehensive investigation in this work, values of sphericity between 0.71 and 1.00 were considered. For consistent comparative analysis, the dimensions of each particle shape were determined maintaining identical particle volume specified by r_{toroid}, the equivalent radius of a sphere with identical volume. This results in the following relationship between the circular toroid dimensions,

$$b_{\text{toroid}} = \sqrt{2r_{\text{toroid}}{}^3/(3\pi a_{\text{toroid}})} \quad (5)$$

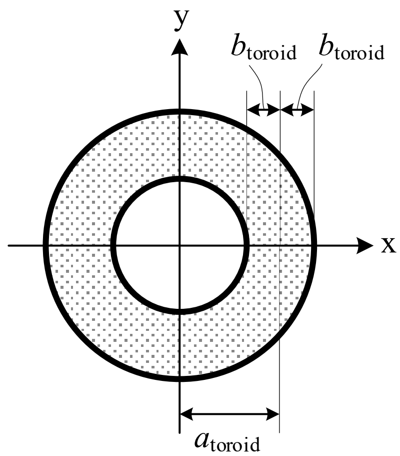

Figure 3: Two-dimensional geometry of a circular toroid.

In commercial software, DEM computational procedures (including the contact model) are usually based on an assumption of spherical particle shape [27]. The simulations in this study were conducted using such code (EDEM [28]) and therefore the multi-sphere approach was used to represent the circular toroid particles. This approach involves rigidly combining many overlapping spheres to create non-spherical shapes and benefits from its use of efficient sphere-based contact computations based on the parameters of the sub-spheres. This approach has been widely adopted in the literature for investigating non-spherical particle dynamics [14,19,29–31]. In addition, previous studies have demonstrated that the variations in particle-scale contact properties do not significantly alter the overall energy dissipation of granular dampers [32]. The further applicability and reliability of the multi-sphere approach has been discussed elsewhere [31,33–36].

As shown in Figure 4, a multi-sphere circular toroid particle can be obtained by lining up a number of identical sub-spheres, whose radius equals to b_{toroid}, along the circular axis of the toroid tube.

Each sub-sphere is identified by the sub-script i, and the sub-spheres are aligned in an anti-clockwise manner with the position of their centroids starting from $\left(x_{\text{sub-sphere},i}, y_{\text{sub-sphere},i}\right) = \left(a_{\text{toroid}}, 0\right)$. The separation angle between two subsequent sub-spheres, $\Delta\varphi_{\text{sub-sphere}}$, determines the number of sub-spheres used, n:

$$n = 2\pi/\Delta\varphi_{\text{sub-sphere}} \tag{6}$$

If $\Delta\varphi_{\text{sub-sphere}} \to 0$, n tends towards infinity which would generate an exact circular toroidal particle. At the other extreme, as each sub-sphere must have physical contact with its neighbours, the criteria for the minimum number of sub-spheres is obtained as:

$$\Delta\varphi_{\text{sub-sphere}} < 2b_{\text{toroid}}/a_{\text{toroid}} \tag{7}$$

By selecting a sufficient separation angle, the centre positions of each sub-sphere are found from:

$$\begin{aligned} x_{\text{sub-sphere},i} &= a_{\text{toroid}} \cos\left(\varphi_{\text{sub-sphere},i}\right) \\ y_{\text{sub-sphere},i} &= a_{\text{toroid}} \sin\left(\varphi_{\text{sub-sphere},i}\right) \end{aligned} \tag{8}$$

where $\varphi_{\text{sub-sphere},i}$ is

$$\varphi_{\text{sub-sphere},i} = (i-1)\Delta\varphi_{\text{sub-sphere}} \tag{9}$$

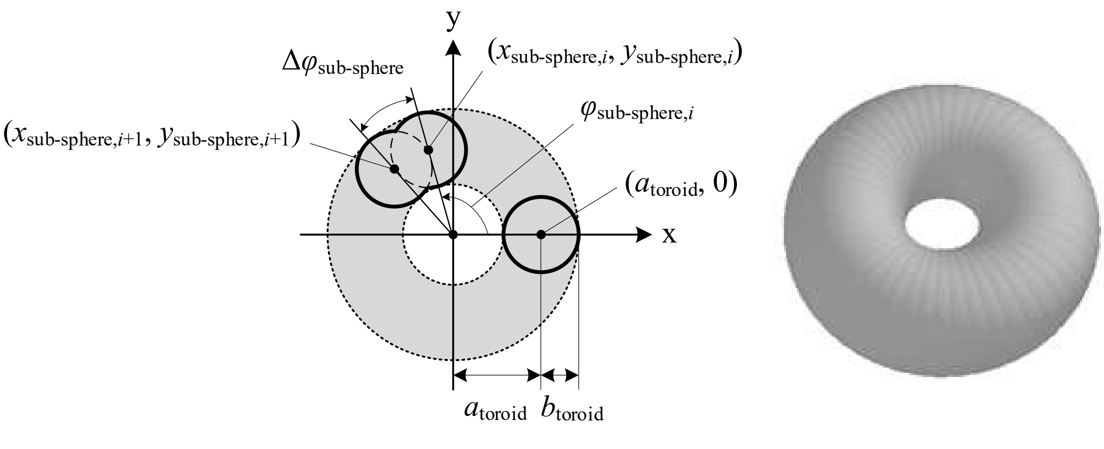

Figure 4: Generation of a circular toroid particle using the multi-sphere approach.

Considering two-dimensional geometry (see xy-plane representation in Figure 4), the proximity of the multi-sphere circular toroid to the perfect geometry was analysed by calculating the area and perimeter errors as the functions of number of sub-spheres as shown in Figure 5. The error curves were obtained for three different dimension ratios. The approximated shape generated the multi-sphere approach underestimates the actual circular toroid area (and hence the volume), and it overestimates the perimeter. The accuracy of the particle shape improves as the number of sub-spheres increase; however, the gain level diminishes for larger numbers of sub-spheres. The error levels are higher for larger circular toroid dimension ratios, i.e., larger holes with respect to overall particle size.

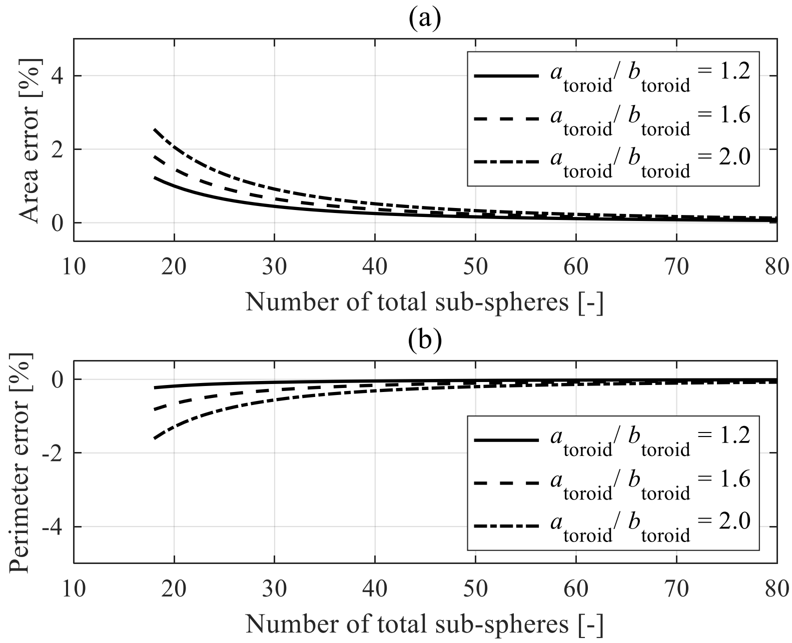

Figure 5: Geometric errors in the multi-sphere circular toroid particles: (a) area and (b) perimeter, where the equivalent sphericities are respectively 0.84, 0.77 and 0.71.

For the DEM simulations, six different numerical particle variations were created using the multi-sphere approach. Note that r_{toroid} was set to 3.5 mm and 50 sub-spheres were judged to be sufficient considering the trade-off between the particle shape accuracy (see Figure 5 for justification) and computational load. This type of non-spherical particle modelling introduces a level of surface roughness. (Note that alternative non-spherical particle modelling methods present different challenges [37]; for example, the use of polyhedra [38] creates sharp edges). While the surface roughness may affect the dynamics of individual particle contacts, its influence on the damper-scale results seems to be limited. Previous work [39] has shown that for a damper containing many 2.5 mm radius particles, a surface roughness of around 12 μm does not significantly alter the time-averaged energy dissipation. For the worst-case situation in this study (sphericity of 0.71) the 50 sub-sphere approximation results in lower levels of roughness, indicating that the multi-sphere approach is appropriate for this work [39].

For the experimental measurement, particles with four levels of sphericity were manufactured using 3D printing technology. A hard acrylic polymer produced from polymethyl methacrylate, was used. This allowed inexpensive manufacturing, minimised magnetic effects, minimised permanent plastic deformations and reduced the computational time step required for DEM simulations [40,41]. Results obtained remain relevant for dampers made from other materials because it has been shown that energy dissipation effectiveness is almost independent of the material type [22,42,43] and any apparent performance dependence relates to density because this affects the total mass of particles and the free space in the enclosure. The manufacturing process was the same as was used successfully in previous work [39].

As a check of accuracy in creating relevant particles, the mass values of simulated and experimental particles are compared with the mass of the reference perfect sphere in Table 1. Mass ratios very close to unity show that the simulated particles are nearly perfect whereas the experimental ones are within 5% of the target.

Table 1: Mass inconsistencies in circular toroid particles with respect to the exact mass of the reference sphere.

Sphericity, ψ	**Measured to nominal mass ratio**	
	Simulation	**Experiment**
0.71	0.996	0.956
0.74	0.996	-
0.78	0.996	0.973
0.83	0.996	-
0.87	1.000	0.947
1.00	1.000	0.987

2.2 Simulation method

In a DEM simulation, the forces acting on each sub-sphere (arising from interactions between individual entities including particles and the enclosure boundaries) are computed along with corresponding deformations. Next, the particle motions are evaluated by solving the Newton-Euler equations of motion at sufficiently small, discretised time steps. A small time step ensures appropriate representation over the duration of each individual contact and therefore achieves an accurate measure of the associated interaction forces and subsequent motions.

In the DEM simulations, it was assumed that interaction forces only arise from inelastic collisions between the entities and slips of the entities on each other. The built-in non-linear Hertz-Mindlin contact model with Coulomb friction [18,31,40,44] was employed between the entities in contact to calculate the elastic and friction components of interaction forces. The inelastic collisional forces were accounted by relating the dissipative elements with the coefficient of restitution [45]. Following this approach, the elastic normal and tangential forces between two contacting surfaces (indexed by 1 and 2) in a simulation were defined by:

$$F_{\text{contact}}^{\text{elastic,normal}}(t) = (4/3)E_{eq}\sqrt{R_{eq}\left(\delta_{\text{contact}}^{\text{normal}}(t)\right)^3} \tag{10}$$

$$F_{\text{contact}}^{\text{elastic,tangential}}(t) = 8G_{eq}\sqrt{R_{eq}\delta_{\text{contact}}^{\text{normal}}(t)}\delta_{\text{contact}}^{\text{tangential}}(t) \tag{11}$$

where ${R_{eq}}^{-1} = {R_1}^{-1} + {R_2}^{-1}$ is the equivalent radius of contact with $R_{1(\text{or } 2)}$ being radius of each surface, ${E_{eq}}^{-1} = (1 - {\upsilon_1}^2){E_1}^{-1} + (1 - {\upsilon_2}^2){E_2}^{-1}$ is the equivalent Young's modulus of contact with $E_{1(\text{or } 2)}$ and $\upsilon_{1(\text{or } 2)}$ respectively being Young's modulus and Poisson's ratio of each surface, ${G_{eq}}^{-1} = (2 - \upsilon_1){G_1}^{-1} + (2 - \upsilon_2){G_2}^{-1}$ is the equivalent shear modulus of contact with $G_{1(\text{or } 2)}$ being shear modulus of each surface. It should be noted that $\delta_{\text{contact}}^{\text{normal}}(t)$ and $\delta_{\text{contact}}^{\text{tangential}}$ represent normal and tangential overlaps of contact at time, *t*, respectively.

Subsequently, the normal dissipative force was expressed as:

$$F_{\text{contact}}^{\text{dis,normal}}(t) = \sqrt{20/3}\Big(\ln(e_{\text{contact}}) /$$

$$\sqrt{(\ln(e_{\text{contact}}))^2 + \pi^2}\Big)\sqrt{m_{eq}E_{eq}\sqrt{R_{eq}\delta_{\text{contact}}^{\text{normal}}(t)}}v_{\text{rel}}^{\text{normal}}(t) \quad (12)$$

where m_{eq} is the equivalent mass of contact with $m_{1(\text{or } 2)}$ being the mass of each contacting body, e_{contact} is the coefficient of restitution (which represents the degree of inelasticity during an impact [46]), and $v_{\text{rel}}^{\text{normal}}(t)$ represents the normal relative velocity of contact at *t*.

For the tangential direction, the dissipative force depended on the sliding/sticking state of contact determined by the Coulomb friction limit. When the elastic tangential force was below the friction force ($\mu_{\text{contact}}F_{\text{contact}}^{\text{elastic,normal}}(t)$ where μ_{contact} is the coefficient of friction), sticking state condition applied, and, thus the tangential dissipative force was calculated by:

$$F_{\text{contact}}^{\text{dis,tangential}}(t) = \sqrt{80/3}\Big(\ln(e_{\text{contact}}) /$$

$$\sqrt{(\ln(e_{\text{contact}}))^2 + \pi^2}\Big)\sqrt{m_{eq}G_{eq}\sqrt{R_{eq}\delta_{\text{contact}}^{\text{normal}}(t)}}v_{\text{rel}}^{\text{tangential}}(t) \quad (13)$$

where $v_{\text{rel}}^{\text{tangential}}(t)$ depicts the tangential relative velocity of contact at *t*.

Otherwise, when the Coulomb friction limit was achieved, sliding state occurred. For this condition, the elastic tangential force was eliminated, and the total tangential force was composed only by the dissipative friction force:

$$F_{\text{contact}}^{\text{dis,tangential}}(t) = \mu_{\text{contact}}F_{\text{contact}}^{\text{elastic,normal}}(t) \quad (14)$$

It should be noted that the contact force expressions above and related kinematics are expressed as scalars. However, the vectorial expressions of those mentioned were achieved by simply multiplying them with the respective contact unit vectors along the normal and tangential directions in the simulation computations.

The energy dissipated in a DEM model from the beginning of a simulation to an arbitrary time, *t*, is obtained by summing up the dissipated energies over each simulation time increment as:

$$E_{\text{numerical}}(t) = \sum_{k=1}^{t/\Delta t} \Delta E_{\text{numerical}}\,(k\Delta t) \tag{15}$$

where Δt is the simulation time step. Assuming that the energy dissipation arises from only the dissipative forces implemented in the contact model, it can be computed at each time step as:

$$\Delta E_{\text{numerical}}(k\Delta t) = \sum_{I=1}^{N_{\text{particle}}} \sum_{i=1}^{N_{\text{sub-sphere,I}}} \sum_{j=1}^{N_{\text{contact,I,i}}} \Big(\mathbf{F}_{\text{contact},I,ij}^{\text{dis,normal}}(k\Delta t) \cdot \mathbf{v}_{\text{rel},I,ij}^{\text{normal}}(k\Delta t) + \mathbf{F}_{\text{contact},I,ij}^{\text{dis,tangential}}(k\Delta t) \cdot \mathbf{v}_{\text{rel},I,ij}^{\text{tangential}}(k\Delta t)\Big) \tag{16}$$

where N_{particle} is the total number of particles in the model, $N_{\text{sub-sphere},I}$ is the number of sub-spheres that construct the corresponding particle, $N_{\text{contact},I,i}$ is the total number of contacts that the corresponding sub-sphere has, $\mathbf{F}_{\text{contact},I,ij}^{\text{dis,normal}}$ and $\mathbf{F}_{\text{contact},I,ij}^{\text{dis,tangential}}$ are respectively normal and tangential dissipative force vectors acting on the corresponding sub-sphere, $\mathbf{v}_{\text{rel},I,ij}^{\text{normal}}$ and $\mathbf{v}_{\text{rel},I,ij}^{\text{tangential}}$ are respectively normal and tangential relative velocity vectors between the corresponding sub-sphere and its related contact.

As the energy dissipation can fluctuate in time depending on the damper) enclosure position in a vibration period, it is more useful to obtain the average energy dissipated over a vibration cycle for consistent analyses. The average energy dissipation per vibration cycle is evaluated as:

$$\tilde{E}_{\text{numerical}} = 2\pi\big(E_{\text{numerical}}(t_1) - E_{\text{numerical}}(t_2)\big)/\big(\omega(t_2 - t_1)\big) \tag{17}$$

where the time points, t_1, t_2, define the energy dissipation computation duration selected within the steady-state vibration and ω is the excitation frequency.

2.3 Experimental method

As shown in Figure 6, an experimental test setup was constructed to allow measuring the energy dissipation of a granular damper under a harmonic excitation. The setup was based on the pioneering work done in Penn State [23]. This setup represents a standard and widely recognised methodology in vibration testing of particle dampers and has been used extensively elsewhere [7,12,14,47,48].

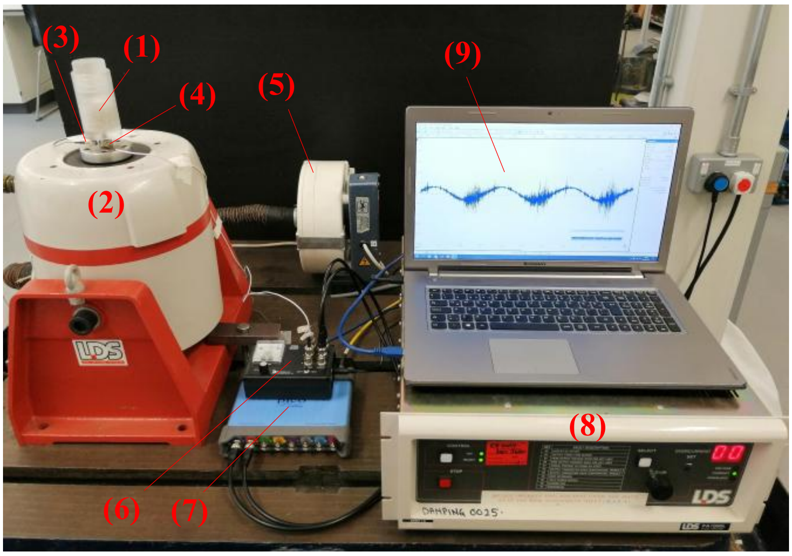

(1) Granular damper
(2) Shaker
(3) Accelerometer
(4) Force transducer
(5) Forced air cooling
(6) Signal conditioner unit
(7) Digital oscilloscope
(8) Power amplifier
(9) PC

Figure 6: Experimental setup for measuring the energy dissipation of a granular damper.

In this setup, the damper enclosure was mounted to the electrodynamic shaker (capable of delivering a peak sine force of 489 N, peak accelerations of 1147 m/s², peak-to-peak displacement of 19 mm) with the armature resonance at 6 kHz to allow the application of harmonic excitations to the damper. The force transducer (with a sensitivity of 22.48 mV/N, a maximum tension limit of 890 N, and a maximum compression limit of 4450 N) was located between the damper enclosure and the shaker to measure the exerted force while the damper undergoes vibrational excitations. To minimise the phase delay associated with movement between the shaker and the damper enclosure, the threaded connections were engaged with sufficient torque and checked regularly. The accelerometer (with a sensitivity of 9.81 mV/g and a measurement range of ±500 g) was bonded to the underside of the enclosure. The forced air cooler was used to exhaust the warm air from the shaker while testing. The excitation function was created digitally using the personal computer and transmitted (first through a digital-to-analogue converter on the oscilloscope and then the power amplifier) to shaker as an analogue signal. When the system was operational, the accelerometer and the force transducer collected the analogue data. These data sets were conditioned by the signal conditioner and then obtained as the digital data by a high-precision oscilloscope (utilising a 20 MHz 12-bit 8-channel oscilloscope). The measured voltage-based signals were converted to the acceleration ($a(t)$) and the force ($f(t)$) using the associated transducer sensitivities, and they were stored by the computer for further processing.

In the experimental setup, the average energy dissipation per cycle (equivalent to the numerically calculated average energy dissipation per cycle in Equation 17) is obtained by evaluating the average of the total mechanical work done by the shaker on the damper over a vibration cycle of steady-state vibrations. It should be noted that during steady-state harmonic excitations, the net mechanical energy injected into the system by the external excitation force (i.e., shaker) over one complete cycle equals the total energy dissipated by the granular damper [23]. This computation is typically performed in frequency-domain by transforming the measured acceleration and force signals into the frequency domain. This transformation allows the velocity spectrums to be simply obtained from the measured acceleration signals without requiring time-domain integration. The average energy dissipation per cycle is given by,

$$\tilde{E}_{\text{experimental}} = 2\pi \operatorname{Re}\left(\sum_{m=0}^{T_{\text{measurement}} f_{\text{sampling}}-1} \mathbf{F}_m \mathbf{V}_m^* /2\right) /\omega \tag{18}$$

where $T_{\text{measurement}}$ is the steady-state vibration period during which the acceleration and force are measured, f_{sampling} is the sampling rate of measurements, $\mathbf{F}_m$ is the complex force and $\mathbf{V}_m^*$ is the complex conjugate of the complex velocity. Supposing that the measured acceleration and force signals are represented as periodic functions, the frequency domain complex force and velocity are determined by applying the discrete Fourier transform as:

$$\mathbf{V}_m = \sum_{p=0}^{T_{\text{measurement}} f_{\text{sampling}}} a(t_p) e^{-\mathrm{j}2\pi mp(T_{\text{measurement}} f_{\text{sampling}} - 1)} / \mathrm{j}\omega_m \tag{19}$$

$$\mathbf{F}_m = \sum_{p=0}^{T_{\text{measurement}} f_{\text{sampling}}} f(t_p) e^{-\mathrm{j}2\pi mp(T_{\text{measurement}} f_{\text{sampling}} - 1)} \tag{20}$$

where t_p is the discrete time points in the measured signals, ω_m is the mth discretised frequency, and j is the imaginary number.

2.4 Damper properties

Figure 7 illustrates the damper used in this study. The geometrical sizes, material properties and contact model parameters utilised in the DEM simulations are summarised in Table 2. These specific values were obtained from previous investigations of similar granular damper systems [7,14,29]. The particles and the enclosure were made from the same base material (acrylic produced from polymethyl methacrylate). Although the particles were 3D printed while the enclosure was machined from extruded rod, in the simulation they were assumed to have the same properties [7,14]. The construction of the physical enclosure was such that its first natural frequency remained higher than 1200 Hz which provided a wide range of excitation frequency without involving the dynamics of enclosure.

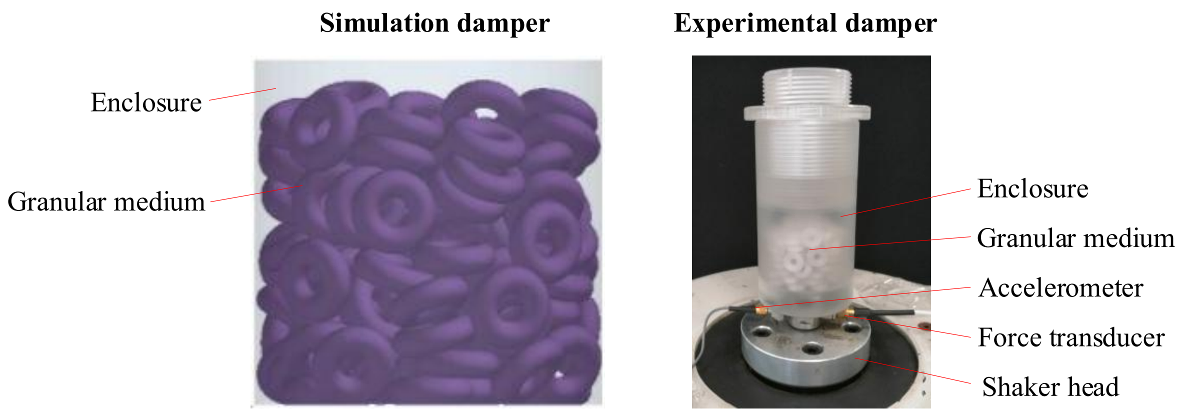

Figure 7: Granular dampers used in simulation and experiment, respectively.

The number and size of the particles and dimensions of the cavity result in a volume fill ratio of 0.39. The clearance within the enclosure depends additionally on packing density which can range from 0.55 to 0.78 [49] depending on the distribution and sphericity of the toroidal particles. To achieve approximately random positions and orientations within the enclosure, for both experiment and simulation, the particles were introduced in an arbitrary manner and allowed to settle naturally under the effect of gravity. In the simulations, the initial settling process time was 0.2 seconds, and the simulation time step was set as 10^{-6} seconds. This time step was selected to be less than 20% of the Rayleigh critical time step approximation [50,51] (5.5×10^{-6} seconds for the sub-spheres of the circular toroidal particle with 0.71 sphericity) for accurate calculation of contact forces. The loading duration of simulations (exposure to the enclosure motion, $u(t)$,) was 18 vibration periods to obtain a sufficient number of steady-state vibration cycles. It was seen in the simulations that most transient effects vanished after 3 vibration periods and, thus, the last 15 periods were used to compute the average dissipated energies. Nevertheless, the simulations were run three times for some particle configurations and loading conditions to ensure that the typical uncertainty levels were insignificant in the estimated dissipated energies.

In the experimental study, when the damper reached steady-state motion, the acceleration and force signals were recorded for 5 seconds. For each measurement, a sampling rate of 40 kHz was used to ensure accurate representation. The particle configurations, repeated in the simulation, were tested three times, following the same procedure, to identify and eliminate any unanticipated uncertainty in the measurements.

Table 2: Main parameters for the particles and enclosure.

Parameter	**Value**
Enclosure diameter	40 mm
Enclosure height	40 mm
Reference particle radius	3.5 mm
Number of particles	110
Density	1190 kg/m^3
Young's modulus	3.3 GPa
Poisson's ratio	0.37
Coefficient of friction, CoF	0.52
Coefficient of restitution, CoR	0.86

3 Results and discussion

3.1 Particle shape dependent energy dissipation efficiency

The effect of the circular toroid particle on the granular energy dissipation efficiency was obtained through parallel numerical discrete element method (DEM) simulations and physical experimental measurements, using the damper configurations described in Section 2. This approach was adopted to ensure that the particle-shape-dependent dissipative behaviour could be characterised and assessed across both methodologies in a consistent manner. While the DEM simulations allow for computation of dissipated energies at particle-scale through internal contact mechanics, the physical experiments provide validation of the numerical results by measuring dissipated energies at damper-scale. Maintaining both methods in this investigation ensures greater confidence in the observed trends. To enable direct comparisons between the numerical predictions and the experimental measurements, the same damper geometry, total particle mass, and volume fill ratio were employed in both the numerical model and the experimental setup.

Figure 8 presents the damping efficiency results as a function of the excitation amplitude for several excitation frequencies ranging from 20 Hz to 160 Hz. These results allow a direct assessment of how the sphericity of a circular toroid particle influences the nonlinear dissipative performance of granular dampers across different dynamic motional phases of the granular medium, particularly for the fluidisation and bouncing-bed optima.

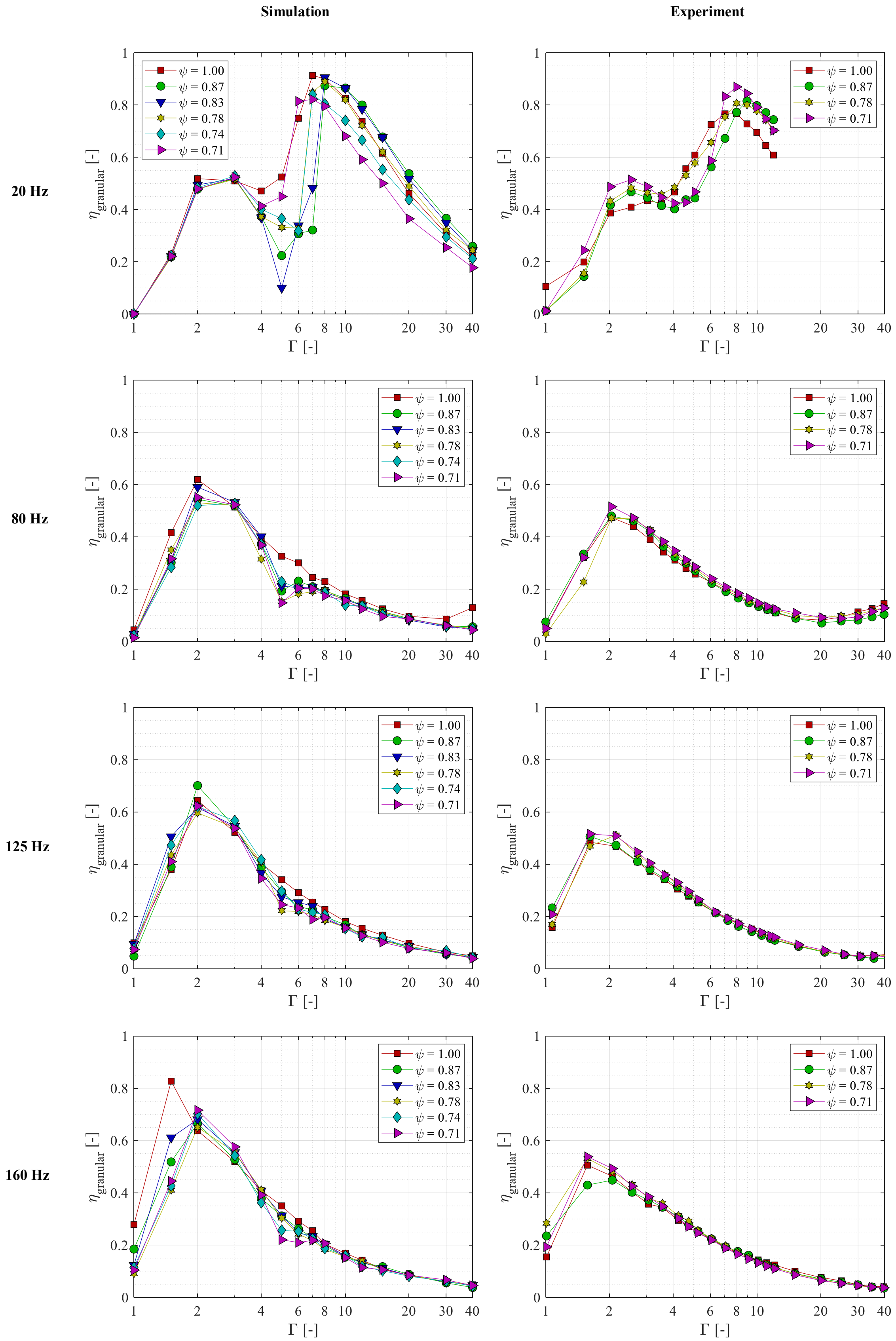

Figure 8: Predicted and measured energy dissipation efficiencies for granular dampers with varying particle sphericity at different vertical excitation frequencies.

At the lowest excitation frequency, i.e., 20 Hz, the results exhibit the general characteristics of a granular damping performance curve: a significant rise of efficiency with increasing excitation intensity from $\Gamma = 1$, followed by a local peak performance around $\Gamma = 2 - 3$ associated with the fluidisation optimum, and a gradual reduction beyond this amplitude. At higher excitation levels, a second but sharper rise in the damping efficiency is observed, ultimately leading to the maximum efficiency corresponding to the onset of the bouncing-bed. Both the numerically predicted and experimentally measured results demonstrate these characteristics for all investigated particle shapes, with the fluidisation and bouncing-bed optima being clearly identifiable in each case.

At excitation frequencies higher than 20 Hz, the form of the damping efficiency curves remains the same for both the numerical and experimental results although parts of the performance curve move outside the investigated amplitude range. As the excitation frequency increases, the excitation amplitudes required to initiate the bouncing-bed phase become higher, and as a result, only the fluidisation optimum is clearly apparent within the amplitude range. For example, at 80 Hz, a slight increase in the damping efficiency is observed near $\Gamma \approx 40$ for spherical particles in numerical simulations and all particle types in experiments, indicating that the granular medium approaches the onset of the bouncing-bed phase, although this condition is not fully reached within the available excitation amplitude range.

From Figure 8 it can be seen that there is a relatively close match between simulation and experiment. Repeat tests (and simulation runs) from random starting conditions and examination of sensitivity to processing parameters suggest that the variability in damping efficiency is less than ±0.05. Based on this, and the spacing between individual data points (see Figure 8), it is reasonable to assume uncertainty of up to 10% in estimates of the height and location (excitation intensity) of the fluidisation and bouncing-bed optima.

3.2 Fluidisation optimum

Figure 8 ($\Gamma < 4$ at 20 Hz and other frequency results) illustrate the influence of circular toroid particle shape on the granular damping efficiency associated with the fluidisation optimum and the transitions between solid, fluid and convection phases. The results indicate that particle sphericity has limited influence on the dissipative behaviour for fluidisation-dominated motion. To enable further comparison, the height and location of the fluidisation optima are presented in Figure 9.

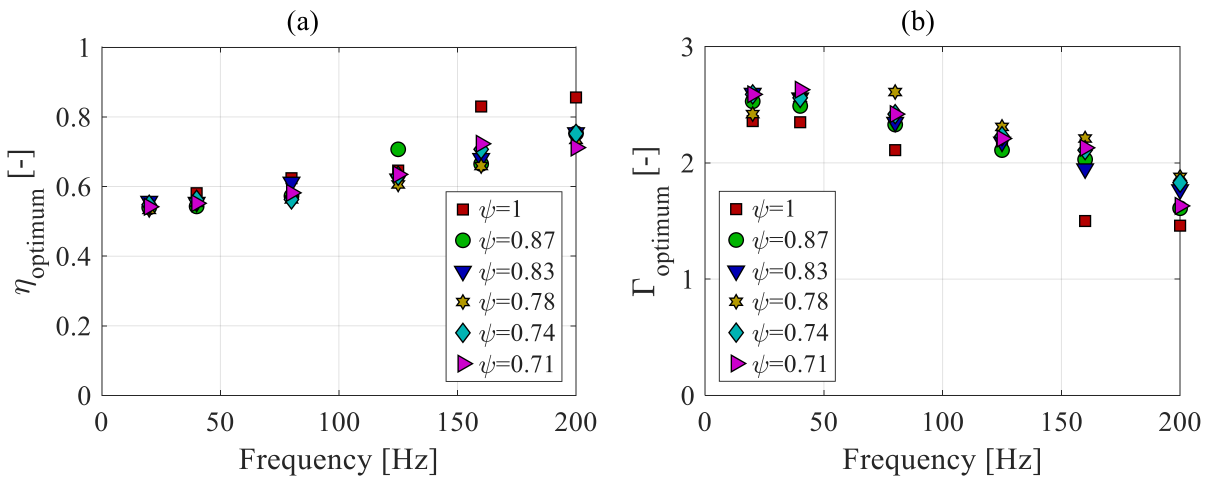

Figure 9: Effect of frequency on efficiency level and amplitude location of fluidisation optimum (using data from the DEM simulation).

At higher frequencies, the fluidisation peak increases in efficiency level somewhat and shifts slightly towards lower acceleration levels. This tendency has been noted elsewhere in the study of granular dampers and is attributed to standing waves within the medium that [29,52,53], for this configuration, could appear below 500 Hz. Under these conditions the actual vibration intensity experienced by the particles may be significantly higher than those experienced by the enclosure walls, allowing fluidisation to take place before the applied excitation reaches normally expected levels.

The effect of particle shape on the fluidisation zone appears to be relatively small: increased sphericity results in greater sensitivity to frequency, but the overall effect barely exceeds the result-to-result variability noted earlier. In this phase, compaction and decompaction occurs each cycle and the underlying energy dissipation mechanisms are primarily controlled by inter-particle surface interactions that produce small-scale frictional dissipation. In the optimal fluidisation condition, the DEM results show that nearly one third of the average kinetic energy involves particle rotation for all shapes considered. While this might suggest that particles with lower sphericity would be subjected to more interactions and therefore a greater retardation in movement, there is no corresponding change in energy dissipation level. The likely reason is that the compaction-decompaction process provides enough space between particles so that contacts occur individually rather than together. Therefore, the effective stiffness of the granular medium, which is sensitive to particle shape in dense particle configurations, plays only a minor role in the dissipation behaviour during the solid-fluid-convection transition.

3.3 Bouncing-bed optimum

The bouncing-bed optimum amplitude exhibits a systematic variation with the sphericity of circular toroid particles, as can be seen in the numerical and experimental 20 Hz results provided in Figure 8. The maximum damping efficiency (height of the peak) remains relatively consistent as the particle shape changes, being around $\eta_{\text{granular}} = 0.8$ for the experiment and $\eta_{\text{granular}} = 0.9$ for the simulation. Note that the tendency for DEM to slightly overestimate damping efficiency has been recorded elsewhere [29,54]. Also, peak efficiency in the bouncing bed appears slightly lower as the optimum approaches the fluidisation optimum amplitude range. This behaviour is attributed to coupling between the bouncing-bed phase and the fluid-convection phase path. When the bouncing-bed optimum occurs close to the tail of the fluid-convection damping efficiency curve, the dissipation mechanism associated with the fluid-convection motional path become increasingly significant, leading to a reduction in the overall efficiency of the bouncing-bed. Conversely, when the bouncing-bed is well separated from the fluid-convection phase, energy dissipation is dominated by collective collisions, resulting in higher damping efficiency.

As the discrete sampling of the excitation amplitudes does not always allow precise location of the optimum amplitudes, Figure 10 presents values approximated by using one-dimensional cubic interpolation around the peaks.

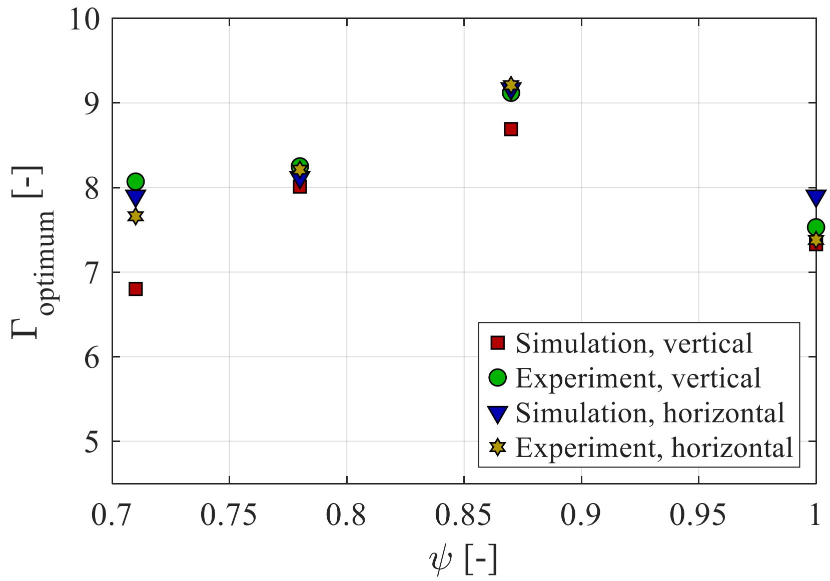

Figure 10: Variation of the bouncing-bed optimum amplitude with particle sphericity.

In Figure 10, the numerical and experimental results together show that the optimum amplitude initially shifts to higher levels as the particle sphericity decreases from $\psi = 1.00$ (perfect sphere) to an intermediate value ($\psi = 0.83$). A further reduction in sphericity causes the optimum amplitude to reduce and approach to a level close to that observed for spherical particles. Note that Figure 10 includes results for horizontal excitation where the entire setup is rotated by 90 degrees with respect to gravity. All four sets of results follow each other closely. The one exception occurs with the vertical simulation at low sphericity – this is discussed further in Section 3.4.

In this motional phase, the particles are locked close together throughout the cycle. Consequently, particle rotation is minimised (rotational kinetic energy is less than 15%) and the packing density instead becomes the important parameter. Deviation from a perfect sphere modifies the packing properties of a granular medium [49]. Specifically, the analytical study data on the dense packing of tori (Figure 4 in [49]) provides direct evidence of a non-monotonic variation in the packing density for the circular toroid shape: particles that are slightly non-spherical allow improved inter-locking and local accommodation of neighbouring particles that can yield a denser packing than perfect spheres, whereas highly non-spherical particles increase open volume in the granular medium leading to higher porosity and lower normal stiffness. This is consistent with the general observation that modest deviations from a true sphere can increase packing density (and porosity, hence stiffness), while larger deviations eventually produce a looser granular medium [30,31,55]. In addition, this mechanistic chain, where particle shape controls packing density, which in turn governs the energy dissipation efficiency, has been also established in a previous study with non-spherical spheroid particles [14].

For the results presented in this work, the actual packing density was measurable from the simulation, using the output mean particle position. Previous work has indicated that the initiation of the bouncing bed phase can be estimated using a simple relationship involving the excitation intensity (amplitude and frequency) and the clearance (distance the particles can travel) within the enclosure [56–58]. This can be written as,

$$\Gamma_{\mathrm{optimum}} = \omega^2 h/(g\pi) \tag{21}$$

where h is the clearance which can be estimated from the volume fill ratio υ and the maximum achievable volume fill ratio υ_{max} using,

$$h = L(1 - \upsilon/\upsilon_{\mathrm{max}}) \tag{22}$$

with υ_{max} being in the range 0.55 to 0.64 for spherical particles depending on packing achieved. Note that L is the length of enclosure along the excitation direction. Estimates (using Equations 21 and 22) based on the actual packing density instead of υ_{max} for spheres are shown in Figure 11 and clearly match the DEM simulations.

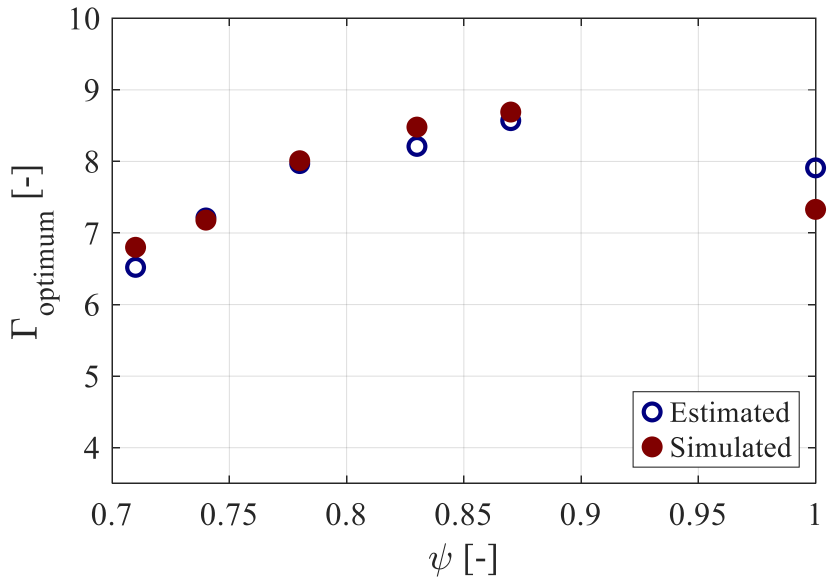

Figure 11: Comparison of $\Gamma_{optimum}$ from DEM simulation and estimated from the quasi-static packing density.

From Figure 11, it can be concluded that $\Gamma_{optimum}$ is set by the actual packing density because it is linked to the clearance and therefore the discrepancies seen in Figure 10 can be explained by reduced packing density at lower sphericity levels.

3.4 Quasi-static force-displacement simulation of particle collections

High packing densities can be achieved in theory and sometimes replicated experimentally via a combination of deliberate particle placement and selected vibration input. In practice, this is unlikely to be the situation for a real damper as it undergoes different loading conditions. For smooth spheres that are small compared with the enclosure geometry, random close packing has been shown to give an adequate estimate [7]. In this work, the particles are neither perfectly smooth nor small, with the ratio of container radius to nominal particle radius to being around 6. Under these conditions lower packing should be expected due to wall effects and increased movement restriction from particle shape and friction. In simulations, the significance of these effects can be estimated from the mean particle position, as demonstrated in Section 3.3. For physical systems however, a quasi-static experiment is a more practical way to measure the resistance to compaction and therefore the likely packing density.

To investigate the feasibility of such an approach, this section uses DEM to simulate a quasi-static force-displacement test, as shown in Figure 12. The primary objective was to evaluate how particle sphericity influences the effective normal and shear stiffness of the granular medium within the specific enclosure and thereby assess whether these stiffness variations are linked to the trends observed in the damping efficiency results.

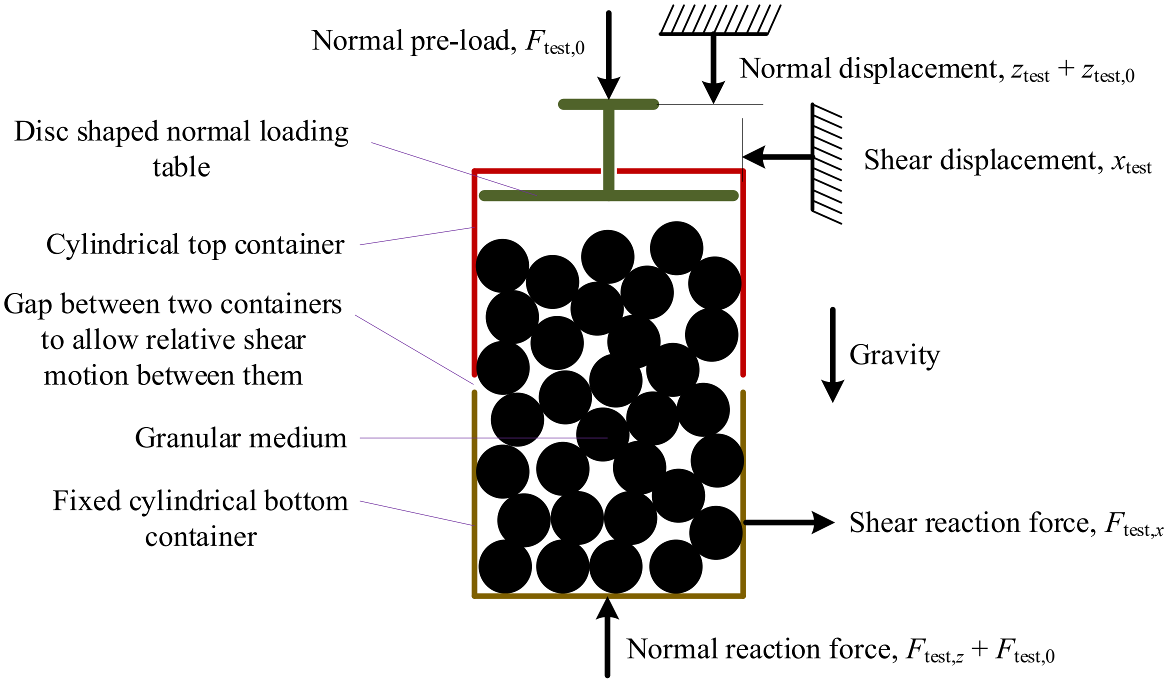

Figure 12: DEM-based force-displacement simulation model for a granular medium.

The model consisted of two identical cylindrical containers (diameter of 40 mm and height of 20 mm) assembled with their open faces opposing each other and separated by a small gap (0.5 mm) to allow shear displacements. The bottom container was set as motionless whilst the top container was used to impose normal (by the disc-shaped table assembled to the top container) and shear displacements (by the top container itself). Particles (100 pieces for each shape) were randomly generated within the void produced by the assembled containers. The key geometric and physical parameters matched those used in the damper. Loading applied was chosen to be of a similar level to that experienced by the particle bed during the vibration tests.

For the normal force-displacement behaviour tests, an initial normal pre-load of 10 N (denoted as $F_{\text{test},0}$ in Figure 12) was applied to prevent sudden particle slips that could result from initial contacts with the loading plate. After recording the initial displacement caused by this pre-load (denoted as $z_{\text{test},0}$ in Figure 12), the quasi-static normal displacement (denoted as z_{test} in Figure 12) was applied via the disc-shaped loading table at a sufficiently low rate to avoid dynamic effects. The reaction force (denoted as $F_{\text{test},z}$ in Figure 12) was measured at the fixed container base resulting from the compression of granular medium and the normal force-displacement results were recorded for each particle shape.

For the shear force-displacement behaviour tests, the granular medium was first subjected to an initial normal pre-load of 50 N to establish a sufficiently compressed granular medium. Subsequently, the quasi-static shear displacement (denoted as x_{test} in Figure 12) was applied to the top container and the reaction shear force (denoted as $F_{\text{test},x}$ in Figure 12) was measured at the fixed container walls exerted by the granular medium.

Characteristic values for quasi-static stiffness were obtained from the gradient of each load-deflection curve. For ease of comparison, the result for each toroidal shape considered was normalised by the stiffness obtained for the equivalent perfect sphere. Figure 13 shows the normalised stiffness plotted against the amplitude at which the bouncing bed was optimised. This is because the optimum amplitude is linked to the packing density, as shown in Equations 21 and 22. Note that each point in Figure 13 relates to a particular level of sphericity. The higher the stiffness, the more densely packed the particles.

The figure shows that there is correlation between quasi-static stiffness and optimum vibration amplitude. In particular, the relationship with shear stiffness is nearly linear, indicating that it is a particularly good to estimate the packing density in the existing conditions, where non-spherical, rough particles are packed into a small container under gravity loading. This finding is consistent with the observation in previous work [14] that static shear stiffness affects the location of the bouncing bed amplitude for significantly non-spherical particles.

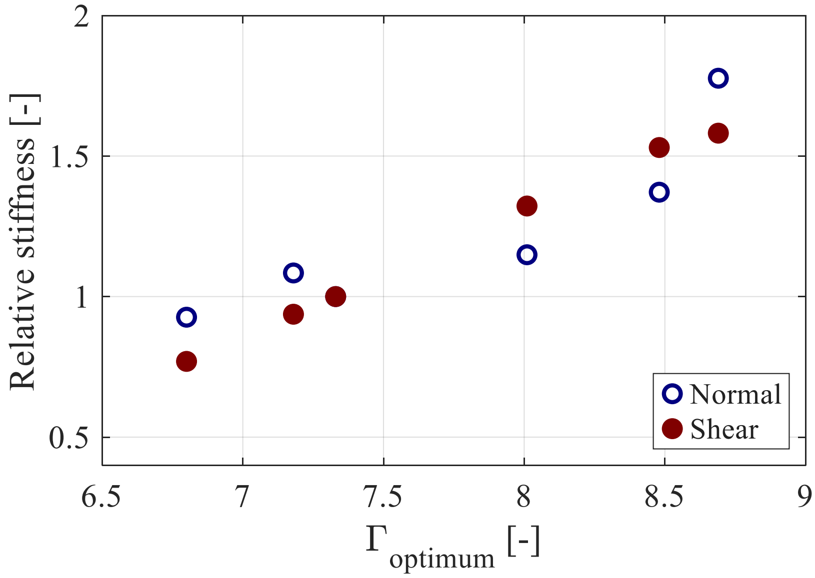

Figure 13: Correlation of bouncing-bed optimum with quasi-static normal and shear stiffness for different levels of sphericity.

3.5 Sphericity and optimum amplitude for the bouncing bed

Both this work using toroidal particles and previous work using spheroidal ones have suggested that the optimum amplitude in the bouncing bed has a non-monotonic relationship with sphericity. Section 3.3 showed that the actual packing density controlled this as it directly affects the clearance according to Equations 21 and 22. By combining these points, it is possible to plot results from different sources together, to show the effect of sphericity on the optimum amplitude. This is presented in Figure 14.

Three sets of data are presented here. The 20 Hz dataset is the same as that shown in Figure 11. Results obtained at 40 Hz were adjusted using Equation 21 to obtain equivalent properties at 20 Hz. The final set were taken from work on spheroids [14] and adjusted using Equation 22 to account for a different packing density (0.41 rather than 0.39).

It can be observed that each set of data follows the same curve, demonstrating consistency in the results and confirming the finding that slightly non-spherical particles cause the optimum to shift to higher amplitudes because of increased packing density. Significantly non-spherical particles are less likely to achieve high packing densities as they hinder particles moving past each other. In some ways, this is a similar effect to what has been reported regarding sensitivity to the coefficient of friction [14,29] where increasing levels have sometimes been shown to alter the conditions for optimum performance.

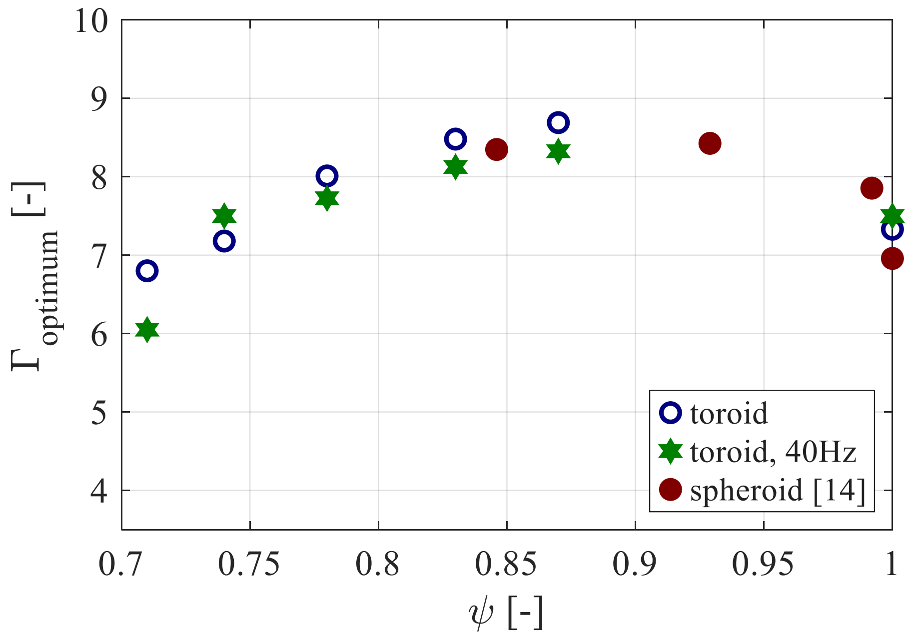

Figure 14: Link between sphericity and optimum bouncing-bed location for different sets of data adjusted to represent 20 Hz excitation with 0.39 volume fill ratio.

4 Conclusions

This paper has investigated the effect of particle shape on granular damping effectiveness using circular toroidal particles of varying sphericity. The work has focused on the important motional phases, namely the bouncing bed and fluidisation, that provide most effective damping. Consistency in the results has been achieved through parallel use of a DEM model and physical experiments.

The work has found that the maximum achievable dissipation effectiveness in both phases is not dramatically altered by particle shape.

The effect of particle sphericity on the fluidisation behaviour is limited. This is because significant cyclic decompaction, but minimal transport occurs at the optimum condition, so dissipation is dominated by small-scale frictional interactions that are only weakly affected by the particle shape. There is evidence to support the hypothesis proposed elsewhere that internal resonances in the granular medium reduce the amplitude required to reach optimum conditions at higher frequencies.

The bouncing-bed phase is where granular damping efficiency is maximised. The excitation amplitude corresponding to the optimum bouncing-bed changes with sphericity, increasing for higher sphericity levels (compared to the optimum for perfect spheres) and then decreasing as sphericity levels are further reduced. The key factor that controls the location of the optimum is the true packing density as this affects the effective clearance within the damper. The packing density is affected by the particle shape, and for smaller enclosures under practical operating conditions, this may be significantly lower than the theoretical values.

In simulations, packing density is relatively easily found although methods used to construct particles could add roughness, thereby retarding the ability of the medium to compact fully. For physical systems, the quasi-static shear stiffness of the granular medium appears to provide a good measure of its packing density. While it is reasonable to expect small smooth spheres in a large container to reach the random close packing density of 0.64, larger particles that are significantly non-spherical achieve less. The relative values of shear stiffness between spherical and non-spherical particles appear to be a good indicator of the packing density.

References

[1] H. V Panossian, Structural damping enhancement via non-obstructive particle damping technique, J. Vib. Acoust. 114 (1992) 101–105. https://doi.org/10.1115/1.2930221.

[2] H. V Panossian, Non-obstructive particle damping: New experiences and capabilities, in: 49th AIAA/ASME/ASCE/AHS/ASC Structures, Structural Dynamics and Materials Conference, Schaumburg, Illinois, 2008. https://doi.org/10.2514/6.2008-2102.

[3] R. Ehrgott, H. V. Panossian, G. Davis, Modeling techniques for evaluating the effectiveness of particle damping in turbomachinery, in: AIAA/ASME/ASCE/AHS/ASC Structures, Structural Dynamics and Materials Conference, Palm springs, California, 2009. https://doi.org/10.2514/6.2009-2690.

[4] F. Duvigneau, S. Koch, E. Woschke, U. Gabbert, An effective vibration reduction concept for automotive applications based on granular-filled cavities, Journal of Vibration and Control 24 (2018) 73–82. https://doi.org/10.1177/1077546316632932.

[5] Y. Badri, G. Dodd, A. Hall, J.E. Cater, G. Schmid, G. Emms, Damping loss factor of granular material mixtures using a coupled finite element-discrete element method, Powder Technol. 464 (2025) 121269. https://doi.org/10.1016/j.powtec.2025.121269.

[6] N. Meyer, R. Seifried, Toward a design methodology for particle dampers by analyzing their energy dissipation, Comput. Part. Mech. 8 (2021) 681–699. https://doi.org/10.1007/s40571-020-00363-0.

[7] F. Terzioglu, J.A. Rongong, C.E. Lord, Motional phase maps for estimating the effectiveness of granular dampers, Mech. Syst. Signal Process. 188 (2023) 110038. https://doi.org/10.1016/j.ymssp.2022.110038.

[8] A. Sack, M. Heckel, J.E. Kollmer, F. Zimber, T. Pöschel, Energy Dissipation in Driven Granular Matter in the Absence of Gravity, Phys. Rev. Lett. 111 (2013) 018001. https://doi.org/10.1103/PhysRevLett.111.018001.

[9] A. Sack, K. Windows-Yule, M. Heckel, D. Werner, T. Pöschel, Granular dampers in microgravity: sharp transition between modes of operation, Granul. Matter 22 (2020) 1–6. https://doi.org/10.1007/s10035-020-01017-x.

[10] Z. Yin, F. Su, H. Zhang, Investigation of the energy dissipation of different rheology behaviors in a non-obstructive particle damper, Powder Technol. 321 (2017) 270–275. https://doi.org/10.1016/j.powtec.2017.07.090.

[11] K. Zhang, T. Chen, X. Wang, J. Fang, Rheology behavior and optimal damping effect of granular particles in a non-obstructive particle damper, J. Sound Vib. 364 (2016) 30–43. https://doi.org/10.1016/j.jsv.2015.11.006.

[12] B. Yao, Q. Chen, Investigation on zero-gravity behavior of particle dampers, Journal of Vibration and Control 21 (2015) 124–133. https://doi.org/10.1177/1077546313488157.

[13] K. Zhang, T. Chen, L. He, Damping behaviors of granular particles in a vertically vibrated closed container, Powder Technol. 321 (2017) 173–179. https://doi.org/10.1016/j.powtec.2017.08.020.

[14] F. Terzioglu, J.A. Rongong, C.E. Lord, Influence of particle sphericity on granular dampers operating in the bouncing bed motional phase, J. Sound Vib. 554 (2023) 117690. https://doi.org/10.1016/j.jsv.2023.117690.

[15] F. Terzioglu, J.A. Rongong, C.E. Lord, Construction of motional phase maps for granular dampers, Internoise 2022 - 51st International Congress and Exposition on Noise Control Engineering 265 (2022) 128–139. https://doi.org/10.3397/in_2022_0025.

[16] C. Salueña, T. Pöschel, S.E. Esipov, Dissipative properties of vibrated granular materials, Phys. Rev. E 59 (1999) 4422–4425. https://doi.org/10.1103/PhysRevE.59.4422.

[17] M.N. Bannerman, J.E. Kollmer, A. Sack, M. Heckel, P. Mueller, T. Pöschel, Movers and shakers: Granular damping in microgravity, Phys. Rev. E 84 (2011) 011301. https://doi.org/10.1103/PhysRevE.84.011301.

[18] K. Mao, M.Y. Wang, Z. Xu, T. Chen, DEM simulation of particle damping, Powder Technol. 142 (2004) 154–165. https://doi.org/10.1016/j.powtec.2004.04.031.

[19] H. Pourtavakoli, E.J.R. Parteli, T. Pöschel, Granular dampers: does particle shape matter?, New J. Phys. 18 (2016) 073049. https://doi.org/10.1088/1367-2630/18/7/073049.

[20] M. Sánchez, C.M. Carlevaro, L.A. Pugnaloni, Effect of particle shape and fragmentation on the response of particle dampers, Journal of Vibration and Control 20 (2014) 1846–1854. https://doi.org/10.1177/1077546313480544.

[21] J.M. Bajkowski, B. Dyniewicz, C.I. Bajer, Damping properties of a beam with vacuum-packed granular damper, J. Sound Vib. 341 (2015) 74–85. https://doi.org/10.1016/j.jsv.2014.12.036.

[22] M. Masmoudi, S. Job, M.S. Abbes, I. Tawfiq, M. Haddar, Experimental and numerical investigations of dissipation mechanisms in particle dampers, Granul. Matter 18 (2016) 1–11. https://doi.org/10.1007/s10035-016-0667-4.

[23] M.Y. Yang, Development of master design curves for particle impact dampers, PhD thesis, The Pennsylvania State University, 2003.

[24] M.Y. Yang, G.A. Lesieutre, S.A. Hambric, G.H. Koopmann, Development of a design curve for particle impact dampers, in: Smart Structures and Materials 2004: Damping and Isolation, Bellingham, WA, 2004: p. 450. https://doi.org/10.1117/12.540019.

[25] I. Cruz-Matías, D. Ayala, D. Hiller, S. Gutsch, M. Zacharias, S. Estradé, F. Peiró, Sphericity and roundness computation for particles using the extreme vertices model, J. Comput. Sci. 30 (2019) 28–40. https://doi.org/10.1016/j.jocs.2018.11.005.

[26] H. Wadell, Volume, Shape, and Roundness of Quartz Particles, J. Geol. 43 (1935) 250–280. https://doi.org/10.1086/624298.

[27] P.A. Cundall, O.D.L. Strack, A discrete numerical model for granular assemblies, Geotechnique 29 (1979) 47–65. https://doi.org/10.1680/geot.1979.29.1.47.

[28] Altair Engineering Inc., EDEM 2021.1, (2021).

[29] F. Terzioglu, J.A. Rongong, Selection of granular damper parameters to achieve optimum vibration attenuation on vibrating structures, Mech. Syst. Signal Process. 229 (2025) 112512. https://doi.org/10.1016/j.ymssp.2025.112512.

[30] P. Parafiniuk, M. Molenda, J. Horabik, Influence of particle shape and sample width on uniaxial compression of assembly of prolate spheroids examined by discrete element method, Physica A: Statistical Mechanics and Its Applications 416 (2014) 279–289. https://doi.org/10.1016/j.physa.2014.08.063.

[31] J. Wiacek, M. Molenda, J. Horabik, J.Y. Ooi, Influence of grain shape and intergranular friction on material behavior in uniaxial compression: Experimental and DEM modeling, Powder Technol. 217 (2012) 435–442. https://doi.org/10.1016/j.powtec.2011.10.060.

[32] M. Sánchez, G. Rosenthal, L.A. Pugnaloni, Universal response of optimal granular damping devices, J. Sound Vib. 331 (2012) 4389–4394. https://doi.org/10.1016/j.jsv.2012.05.001.

[33] D. Markauskas, R. Kačianauskas, A. Džiugys, R. Navakas, Investigation of adequacy of multi-sphere approximation of elliptical particles for DEM simulations, Granul. Matter 12 (2010) 107–123. https://doi.org/10.1007/s10035-009-0158-y.

[34] M. Pasha, C. Hare, M. Ghadiri, A. Gunadi, P.M. Piccione, Effect of particle shape on flow in discrete element method simulation of a rotary batch seed coater, Powder Technol. 296 (2016) 29–36. https://doi.org/10.1016/j.powtec.2015.10.055.

[35] M. Alizadeh, A. Hassanpour, M. Pasha, M. Ghadiri, A. Bayly, The effect of particle shape on predicted segregation in binary powder mixtures, Powder Technol. 319 (2017) 313–322. https://doi.org/10.1016/j.powtec.2017.06.059.

[36] W. Nan, M. Pasha, T. Bonakdar, A. Lopez, U. Zafar, S. Nadimi, M. Ghadiri, Jamming during particle spreading in additive manufacturing, Powder Technol. 338 (2018) 253–262. https://doi.org/10.1016/j.powtec.2018.07.030.

[37] W. Zhong, A. Yu, X. Liu, Z. Tong, H. Zhang, DEM/CFD-DEM Modelling of Non-spherical Particulate Systems: Theoretical Developments and Applications, Powder Technol. 302 (2016) 108–152. https://doi.org/10.1016/j.powtec.2016.07.010.

[38] J. Chen, Discrete element method for 3D simulations of mechanical systems of non-spherical granular materials, PhD, The University of Electro-Communications, 2012.

[39] F. Terzioglu, J.A. Rongong, C.E. Lord, The effect of particle surface roughness on granular energy dissipation performance, in: Proceedings of the International Congress on Acoustics, Gyeongju, South Korea, 2022. https://eprints.whiterose.ac.uk/194344/.

[40] H. Chen, Y.G. Xiao, Y.L. Liu, Y.S. Shi, Effect of Young's modulus on DEM results regarding transverse mixing of particles within a rotating drum, Powder Technol. 318 (2017) 507–517. https://doi.org/10.1016/j.powtec.2017.05.047.

[41] S. Lommen, D. Schott, G. Lodewijks, DEM speedup: Stiffness effects on behavior of bulk material, Particuology 12 (2014) 107–112. https://doi.org/10.1016/j.partic.2013.03.006.

[42] K.S. Marhadi, V.K. Kinra, Particle impact damping: Effect of mass ratio, material, and shape, J. Sound Vib. 283 (2005) 433–448. https://doi.org/10.1016/j.jsv.2004.04.013.

[43] Z. Lu, S.F. Masri, X. Lu, Parametric studies of the performance of particle dampers under harmonic excitation, Struct. Control Health Monit. 18 (2011) 79–98. https://doi.org/10.1002/stc.359.

[44] A. Di Renzo, F.P. Di Maio, Comparison of contact-force models for the simulation of collisions in DEM-based granular flow codes, Chem. Eng. Sci. 59 (2004) 525–541. https://doi.org/10.1016/j.ces.2003.09.037.

[45] Y. Tsuji, T. Tanaka, T. Ishida, Lagrangian numerical simulation of plug flow of cohesionless particles in a horizontal pipe, Powder Technol. 71 (1992) 239–250. https://doi.org/10.1016/0032-5910(92)88030-L.

[46] W.J. Stronge, Impact Mechanics, Second, Cambridge University Press, New York, 2018.

[47] Y. Duan, Q. Chen, Simulation and experimental investigation on dissipative properties of particle dampers, Journal of Vibration and Control 17 (2011) 777–788. https://doi.org/10.1177/1077546309356183.

[48] H. Guo, R. Yoneoka, A. Takezawa, Influence of cavity partition on the damping performance of additively manufactured particle dampers, Powder Technol. 439 (2024) 119675. https://doi.org/10.1016/j.powtec.2024.119675.

[49] R. Gabbrielli, Y. Jiao, S. Torquato, Dense periodic packings of tori, Phys. Rev. E 89 (2014) 022133. https://doi.org/10.1103/PhysRevE.89.022133.

[50] S. Bin Yeom, E.-S. Ha, M.-S. Kim, S.H. Jeong, S.-J. Hwang, D.H. Choi, Application of the Discrete Element Method for Manufacturing Process Simulation in the Pharmaceutical Industry, Pharmaceutics 11 (2019) 414. https://doi.org/10.3390/pharmaceutics11080414.

[51] M. Marigo, E.H. Stitt, Discrete element method (DEM) for industrial applications: Comments on calibration and validation for the modelling of cylindrical pellets, KONA Powder and Particle Journal 32 (2015) 236–252. https://doi.org/10.14356/kona.2015016.

[52] B. Darabi, J.A. Rongong, Polymeric particle dampers under steady-state vertical vibrations, J. Sound Vib. 331 (2012) 3304–3316. https://doi.org/10.1016/j.jsv.2012.03.005.

[53] B. Darabi, J.A. Rongong, T. Zhang, Viscoelastic granular dampers under low-amplitude vibration, Journal of Vibration and Control 24 (2018) 708–721. https://doi.org/10.1177/1077546316650098.

[54] C.X. Wong, M.C. Daniel, J.A. Rongong, Energy dissipation prediction of particle dampers, J. Sound Vib. 319 (2009) 91–118. https://doi.org/10.1016/j.jsv.2008.06.027.

[55] A.G. Athanassiadis, M.Z. Miskin, P. Kaplan, N. Rodenberg, S.H. Lee, J. Merritt, E. Brown, J. Amend, H. Lipson, H.M. Jaeger, Particle shape effects on the stress response

of granular packings, Soft Matter 10 (2014) 48–59. https://doi.org/10.1039/c3sm52047a.

[56] A. Sack, M. Heckel, J.E. Kollmer, F. Zimber, T. Pöschel, Energy dissipation in driven granular matter in the absence of gravity, Phys. Rev. Lett. 111 (2013) 1–5. https://doi.org/10.1103/PhysRevLett.111.018001.

[57] N. Meyer, R. Seifried, Toward a design methodology for particle dampers by analyzing their energy dissipation, Comput. Part. Mech. (2020). https://doi.org/10.1007/s40571-020-00363-0.

[58] A. Sack, K. Windows-Yule, M. Heckel, D. Werner, T. Pöschel, Granular dampers in microgravity: sharp transition between modes of operation, Granul. Matter 22 (2020) 1–6. https://doi.org/10.1007/s10035-020-01017-x.